The experimental normalized cross-covariance with no delay, $\hat{\rho}(\tau = 0)$, is plotted against the transmission probability, p, of the input point contact (Fig. 2). As the point contact width is increased, the transmission p through the contact increases and the input electron flux to the beam splitter carries less (current-normalized) noise. The experimental cross-covariance coefficient approaches –1 as p increases, in close agreement with the analytical trace calculated using Eq. 5.

The results are shown for the experimental normalized cross-covariance, $\hat{\rho}(\tau)$, as a function of the delay time at four different conductances, $p = G/G_Q = 0.83$, 0.77, 0.71, and 0.61 (Fig. 3). The values of the experimental cross-covariance at $\tau = 0$ in Fig. 3 are identical to those shown in Fig. 2. As the relative delay between the two output channels is increased, the experimental cross-covariance increases toward zero. The characteristic shape of the experimental cross-covariance data is a direct consequence of the bandpass filter (2 to 10 MHz) used in the measurement circuit (*14*). The additional traces shown are from a numerical simulation which accounts for the point contact transmission p, the beam splitter transmission T, and the entire detection circuit, and closely match the experimental data in all four cases. We emphasize that no fitting parameters have been used in either Fig. 2 or 3 to match the theoretical and simulated traces with the experimental data. Furthermore, the results shown are consistent with the coherent-scattering formalism for calculating current-noise correlations (*15*).

The negative cross-covariance of the output currents of the mesoscopic electron beam splitter directly indicates the sub-Poisson (antibunching) fluctuations of the thermal fermion source. The experimental technique we present is simple and clean. It may prove useful in the measurement of electron current covariance in other mesoscopic systems (*16*), for example, in the study of the statistics of entangled electrons (*17*). One might also use this quantum electron optics technique to probe the source statistics of composite particles in other condensed matter systems, such as the quasi-particles in the fractional quantum Hall regime (*18*), the Cooper pairs in superconductors (*19*), and the excitons in semiconductors (*20*).

References and Notes

1. R. Hanbury Brown and R. Q. Twiss, *Nature* **178**, 1447 (1956).
2. E. M. Purcell, *ibid.*, p. 1449.
3. M. Büttiker, *Phys. Rev. Lett.* **65**, 2901 (1990); *Physica B* **175**, 199 (1991); T. Martin and R. Landauer, *Phys. Rev. B* **45**, 1742 (1992).
4. R. Hanbury Brown and R. Q. Twiss, *Nature* **177**, 27 (1956).
5. G. A. Rebka Jr. and R. V. Pound, *ibid.* **180**, 1035 (1957); H. J. Kimble, M. Dagenais, L. Mandel, *Phys. Rev. Lett.* **39**, 691 (1977); F. Diedrich and H. Walther, *ibid.* **58**, 203 (1987); M. Koashi, K. Kono, T. Hirano, M. Matsuoka, *ibid.* **71**, 1164 (1993); J. Kim, O. Benson, H. Kan, Y. Yamamoto, *Nature* **397**, 500 (1999).
6. M. Henny *et al.* [*Science* **284**, 296 (1999)] have realized independently the Hanbury Brown and Twiss experiment.
7. R. E. Burgess, *Discuss. Faraday Soc.* **28**, 151 (1959).
8. This type of relationship is often referred to as the cross-correlation of two signals. Strictly speaking, the normalized cross-correlation and the normalized cross-covariance are identical only in the case of zero-mean signals. Here, they are identical.
9. M. P. Silverman, *Phys. Lett. A* **120**, 442 (1987).
10. B. J. van Wees *et al.*, *Phys. Rev. Lett.* **60**, 848 (1988); D. A. Wharam *et al.*, *J. Phys. C* **21**, L209 (1988).
11. R. C. Liu, B. Odom, Y. Yamamoto, S. Tarucha, *Nature* **391**, 263 (1998).
12. M. Reznikov, M. Heiblum, H. Shtrikman, D. Mahalu, *Phys. Rev. Lett.* **75**, 3340 (1995); A. Kumar, L. Saminadayar, D. C. Glattli, Y. Jin, B. Etienne, *ibid.* **76**, 2778 (1996).
13. Attenuators were used to match the amplifier gains. Bandpass filters (2 to 10 MHz) eliminated spurious noise at frequencies $f \leq 500$ kHz and matched the high-frequency cutoffs of the amplifiers. Delay lines (0 to 128 ns) were used as necessary for the cross-covariance measurement. The signals were resolved using a hybrid mixer with sum and difference outputs, envelope detectors (square-law devices), and lock-in amplifiers; an ac-modulation scheme was used to improve the signal-to-noise ratio over the thermal noise of the amplifiers. See also (*11*, *12*).
14. Ideally, a broad-band measurement circuit would yield a cross-covariance signal containing frequency components from 0 Hz to a high-frequency cutoff of ~100 GHz (the inverse of the electron emission time). Such an ideal cross-covariance signal (plotted versus τ in nanoseconds) would appear to have a very sharp, delta-like anticorrelation at $\tau = 0$ and would quickly go to zero for $\tau \neq 0$. However, cutting off all frequency components higher than 10 MHz creates a sinc-like oscillatory behavior with a center lobe full width at half maximum $FWHM \approx 100$ ns; this is the inverse of the cutoff frequency 10 MHz. Removing the low-frequency components below 2 MHz introduces a slow dc offset modulation with period ≈ 500 ns, which is manifest in Fig. 3 as an apparent side-lobe dc offset. To the extent that the beam splitter device operates in the linear regime (no frequency mixing), $\hat{\rho}(\tau = 0)$ depends only on the input and beam splitter statistics, regardless of the bandwidth used, because the cross-covariance is normalized by the variances of the filtered stationary signals from the outputs (ports 2 and 3).
15. M. Büttiker, *Phys. Rev. B* **46**, 12458 (1992).
16. Ya. M. Blanter and M. Büttiker, *ibid.* **56**, 2127 (1997); S. A. van Langen and M. Büttiker, *ibid.*, p. 1680; T. Gramespacher and M. Büttiker, *Phys. Rev. Lett.* **81**, 2763 (1998).
17. D. P. DiVincenzo and D. Loss, abstract available at http://xxx.lanl.gov/abs/cond-mat/9901137
18. L. Saminadayar, D. C. Glattli, Y. Jin, B. Etienne, *Phys. Rev. Lett.* **79**, 2526 (1997); R. de-Picciotto *et al.*, *Nature* **389**, 162 (1997).
19. M. J. M. de Jong and C. W. J. Beenakker, *Phys. Rev. B* **49**, 16070 (1994); S. Datta, P. Bagwell, M. P. Anantram, *Phys. Chem. Mater. Low-Dimensional Struct.* **3**, 1 (1996).
20. A. Imamoḡlu and R. J. Ram, *Phys. Lett. A* **214**, 193 (1996).

21. We gratefully acknowledge S. Machida for contributions to the cross-correlation circuit and S. Tarucha for contributions to the beam splitter device. W.D.O. gratefully acknowledges continuing support from the National Defense Science and Engineering Graduate Fellowship Program.

7 December 1998; accepted 1 March 1999

The Robust Australopithecine Face: A Morphogenetic Perspective

Melanie A. McCollum

The robust australopithecines were a side branch of human evolution. They share a number of unique craniodental features that suggest their monophyletic origin. However, virtually all of these traits appear to reflect a singular pattern of nasomaxillary modeling derived from their unusual dental proportions. Therefore, recent cladistic analyses have not resolved the phylogenetic history of these early hominids. Efforts to increase cladistic resolution by defining traits at greater levels of anatomical detail have instead introduced substantial phyletic error.

Robust australopithecines are conventionally sorted into three species: a single species from South Africa, *Australopithecus robustus* [1.8 to 1.5 million years ago (Ma)] (*1*), and in East Africa, *A. aethiopicus* (2.7 to 2.3 Ma) and *A. boisei* (2.3 to 1.3 Ma) (*2*). All are characterized by extreme postcanine megadontia, premolars with molarized roots, lower molars with accessory cuspules, and thick molar enamel. All also have sagittal and compound temporal/nuchal extracranial crests, a zygomatic arch positioned high above the occlusal plane, a forward placement of the zygoma, and a robust mandible with an absolutely and relatively tall ramus and a correspondingly tall posterior face (Fig. 1). Robust australopithecines also display markedly small incisors and canines, a thickened hard palate (that part of the upper jaw formed by the palatine process of the maxilla and the horizontal plate of the palatine), a vertically tall infraorbital region, low infraorbital foramina, a face hafted high onto the neurocranium, a frontal region depressed behind the supraorbital torus and between anteriorly converging temporal lines [the frontal trigone (*3*)], and strong postorbital constriction.

Department of Anatomy, Case Western Reserve University, 10900 Euclid Avenue, Cleveland OH 44106, USA. E-mail: mam17@po.cwru.edu

Many of these features are not unique to the robust australopithecines. For example, *A. africanus* shares large second and third molar crowns, a vertically tall mandibular ramus, and, as compared to the more primitive condition displayed by *A. afarensis*, a somewhat more forward placement of the zygoma (*4*). A fragmentary *Homo rudolfensis* sample from East Africa also shows postcanine megadontia (though not as extreme as in robust australopithecines), molarized premolar roots, and thick enamel (*5*, *6*). This repetitious pattern of postcanine megadontia in early hominids has frustrated attempts to resolve their phylogenetic history. Recently, impressive lists of craniodental features shared by robust australopithecines have been cited as overwhelming evidence in support of their monophyletic origin (*6*, *7*). Unfortunately, simply defining a character does not constitute evidence that it is independent and not the incidental effect of another. Which of the robust australopithecine features are truly independent? Resolution of these kinds of issues requires consideration of (i) the underlying genetic program that is ultimately responsible for their morphology and (ii) the process by which that program is interpreted and expressed.

Recent findings from developmental biology have demonstrated that homologous developmental pathways occur in a variety of embryonic processes and organisms, but within discrete units or modules (*8*, *9*). Such modules display a number of distinct properties (*9*). They (i) have an autonomous genetically isolated organization, (ii) contain hierarchical units and may be parts of others, (iii) occupy specific physical locations within the developing system, (iv) exhibit varying degrees of connectivity to other modules, and (v) undergo sequential transformations during individual development. Modules span a hierarchy from molecules to organ primordia and body segments, in such a way that a single complex anatomical structure (for example, the tetrapod forelimb or the vertebrate skull) can be viewed as the independent product of a hierarchical expression of individual embryonic units. Changes either in the attributes of individual modules (state, number, or location) or in the timing of their interactions with one another alter the way organisms develop, and result in modified sets of features being presented to the filtering action of natural selection.

Fig. 1. Characteristic features of the robust australopithecine face. 1, Vertically elongated infraorbital region; 2, low position of the infraorbital foramina; 3, high hafting of face onto neurocranium; 4, frontal trigone; 5, vertically tall mandibular ramus and posterior face; 6, sagittal crest; and 7, anteriorly placed zygomae ("dished" face).

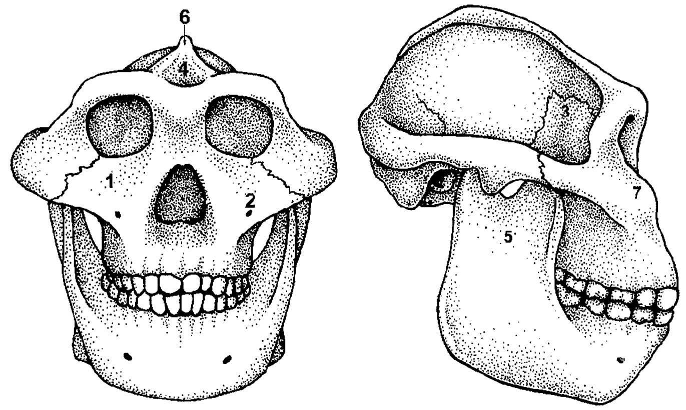

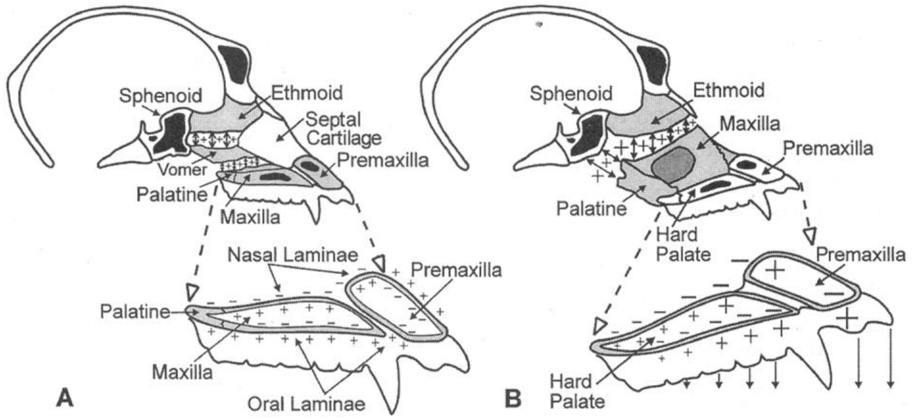

Fig. 2. Principles of facial growth. (**A**) Displacement of the vomer away from its contacts with the perpendicular plate of the ethmoid and hard palate. Sutural deposition in the "spaces" created by this displacement permanently relocates the hard palate and upper jaw inferiorly. The detail of the upper jaw illustrates the independent remodeling and inferior drift of the nasal and oral laminae of the hard palate (maxilla plus palatine) and premaxilla. Plus signs indicate deposition; minus signs indicate resorption. (**B**) Vertical growth of the mandibular condyle displaces the posterior maxilla and hard palate inferiorly, thus eliciting relatively greater bone deposition at the sphenopalatine and posterior ethmomaxillary sutures. The detail illustrates remodeling activities and cortical drift associated with maxillary rotation. Plus signs indicate deposition; minus signs indicate resorption; downward-pointing arrows indicate drift. Symbol size reflects the relative extent and degree of remodeling activity (remodeling and drift). Black areas are air sinuses.

The skull arises and matures as part of an integrated complex of relatively independent functional modules (*10*, *11*). Each consists of all of the tissues, organs, glands, spaces, and supportive structures necessary to carry out a single function (such as mastication, respiration, or olfaction). Like genetically defined embryonic modules, the functional modules of the skull are readily definable, are relatively autonomous [in terms of both development and evolution (*11*)], and interact with one another within a developmental cascade. Much of the adult craniofacial form can therefore be understood with reference to the independent function (but integrated development) of (i) the brain and its associated sensory capsules, (ii) the nasal airway, and (iii) the oral apparatus (*11*, *12*).

The integration of functional modules is achieved through growth remodeling and displacement. Growth remodeling is bone deposition and resorption on the endosteal and periosteal surfaces of bony laminae by the osteoblasts and osteoclasts that reside in their surface membranes (*13*). Such active growth is regulated by the endosteum and periosteum, whose activities are themselves mediated by signals (mechanical, electrical, hormonal, chemical, and so on) received from adjacent tissues. As an example, the hard palate is the structural interface between the nasal and oral cavities, and it therefore consists of functionally independent nasal and oral surfaces (Fig. 2A) (*14*). In response to signals received from the growing tissues of the nasal cavity, the nasal surface (lamina) of the hard palate drifts downward through a combined process of resorption on its outer surface and deposition on its inner surface. Similarly, the oral surface (lamina) of the hard palate drifts inferiorly (through the combined processes of periosteal deposition and endosteal resorption) in response to signals from the growing and functioning oral tissues (Fig. 2A). Ancillary to this active downward relocation of the two palatal surfaces is their passive downward and forward displacement in association with sutural growth. With expansion of the nasal tissues, the bony vomer is displaced away from its articulations with the perpendicular plate of the ethmoid superiorly and the hard palate inferiorly (Fig. 2A). In response to the tension within the sutures created by this displacement (*13*), bone is deposited at the vomeroethmoidal and vomeromaxillary sutures, and the hard palate is relocated downward and anterior to the cranial base. Additional sutural growth associated with expansion of the neuro-orbital and oral cavities displaces the hard palate even farther downward and forward.

The distinctive cranial morphotype of robust australopithecines must ultimately be interpretable in the context of growth remodeling and displacement. With respect to their distinctive palatal morphology, the traditional view holds that a thickened palate developed in response to some mechanical demand, and in particular in response to the need to reinforce the midpalatal suture against elevated masticatory stress (*15*). However, experimental studies demonstrate that an increase in sutural area in response to elevated extrinsic force is achieved through increased interdigitation rather than the accumulation of thick cortical bone (*16*). Thus, a thickened palate must be a function of some other constraint on rostral form. The unusual palatal morphology characteristic of the robust taxa may instead be a product of extreme maxillary rotation during ontogeny (*17*). Maxillary rotation is a normal aspect of anthropoid facial ontogeny (*18*). It results from differential growth of the sutures that attach the midface to the basicranium [the sphenopalatine and ethmomaxillary sutures (Fig. 2B)]. Relatively greater sutural deposition posteriorly typically occurs in order to maintain functional occlusion as the mandibular condyle expands vertically (*13*, *18*). To keep pace with the skeletal changes taking place posteriorly, the anterior hard palate (both laminae) and premaxilla (forming the anteriormost nasal cavity floor and holding the incisors) undergo relatively greater remodeling, and the entire anterior midface and dentition drift downward (Fig. 2B).

In the robust australopithecines, an unusually tall mandibular ramus would have been associated with an extreme degree of maxillary rotation during ontogeny (*19*). Inferior drift of the oral surface of the hard palate would ultimately be determined by the height of the mandibular ramus and the extent of this rotation. Drift of the hard palate's nasal surface, however, would be regulated primarily by the size of the nasal airway, itself a parameter that is largely determined by body size (*12*). Because mandibular ramus height in the robust australopithecines far exceeds that of other hominoids of similar body size (*20*), a general thickening of the hard palate (a gradual separation of its nasal and oral surfaces) would occur. Indeed, this is precisely what occurs in modern chimpanzees, in which an increase in the height of the posterior midface is accompanied by a dramatic thickening of the hard palate and its concurrent invasion by the maxillary air sinus (Fig. 3) (*21*). The fact that palatal morphogenesis in the robust australopithecines was similar to that of the chimpanzee is indicated by the presence of a palatal component of the maxillary sinus, a "recessus palatinus," in several robust australopithecine crania (*3*, *17*). In addition, palatal thickness values of the fossil crania are those that would be expected in chimpanzees with posterior midfaces "grown up" to robust australopithecine size (Fig. 3). Therefore, the thickened hard palate of the robust australopithecines would appear to be a simple by-product of a vertically expanded mandibular ramus.

Australopithecus africanus also displays a relatively tall mandibular ramus suggestive of extreme maxillary rotation (*20*), and although some specimens, including the famous Taung child, possess a recessus palatinus (*22*), adult palatal thickness in this taxon rarely approaches that typical of the robust taxa (Fig. 3). The *A. africanus* morphology therefore suggests that some additional factors may have promoted palatal thickening in robust crania or deterred extreme palatal thickening in nonrobust crania such as *A. africanus* (or both).

Growth remodeling of the nasal surface of the hard palate is regulated almost exclusively by the spatial demands of the nasal cavity (*13*). In comparison, the nasal surface of the premaxilla (Fig. 2) must satisfy not only the requirements of the nasal cavity but also those of the permanent incisors developing within it. Consequently, the resorptive capacity of the premaxilla is more restricted than that of the hard palate. In *A. africanus*, the vomer only contacts the nasal cavity floor at the hard palate (Fig. 4A) (*23*). There it projects below the premaxilla and into the incisive canal (the communicating passage between the nasal and oral cavities). This isolation of the vomer from the premaxilla provides some developmental (remodeling) independence of the two components of the nasal cavity floor. As a result, resorption of the hard palate's nasal surface could continue even after the resorptive limits of the premaxilla had been reached. Unlike the arrangement in *A. africanus*, the vomer of the robust australopithecines

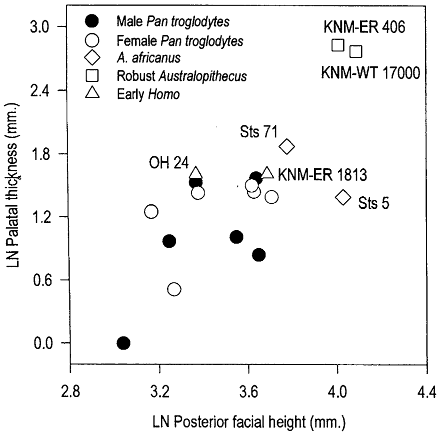

Fig. 3. Palatal thickness compared to posterior facial height in an ontogenetic series of chimpanzees and a number of early hominid crania. LN, natural log. Chimpanzee data points represent sex-specific means (n = 68) of developmental age groups defined by stage of dental eruption and suture closure (deciduous → M^1 erupted → M^2 erupted → M^3 erupted → patent spheno-occipital synchondrosis → fused spheno-occipital synchondrosis). Posterior facial height is measured as the vertical distance separating the articular eminence from the occlusal plane. Number and letter designations beside data points indicate museum accession numbers of fossil crania.

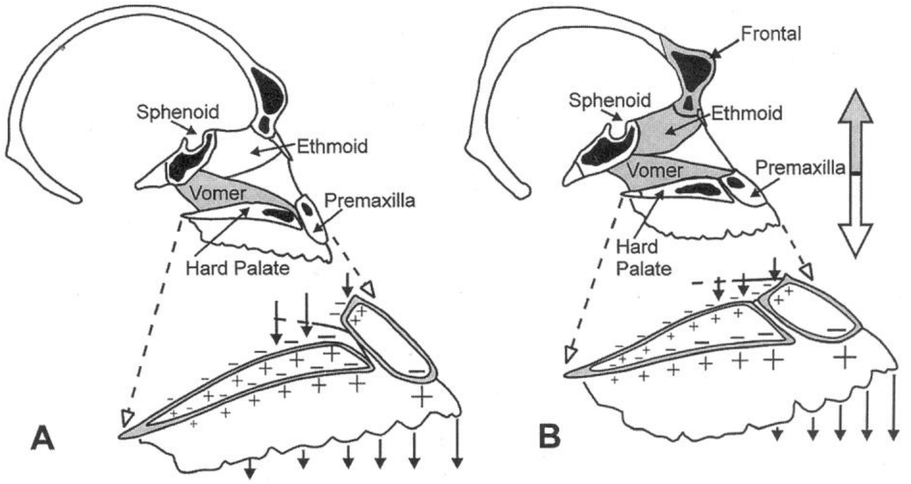

Fig. 4. Proposed variation in nasomaxillary modeling and craniofacial morphogenesis in australopithecine taxa. (**A**) Isolation of the vomer from the premaxilla in *A. africanus* allows continued resorption of the palatal component of the nasal cavity floor after the resorptive limits of the premaxilla have been reached. (**B**) Extension of the vomer onto the premaxilla reduces the resorptive capacity of the palatal component of the nasal cavity floor. With inferior drift of the nasal floor thus constrained, orbitonasal and oral cavities become displaced in opposite directions (large arrows at right). Plus signs indicate deposition; minus signs indicate resorption; downward-pointing arrows indicate drift. Symbol size reflects the relative extent and degree of activity (remodeling and drift). Black areas are air sinuses.

Table 1. Synapomorphies of *Paranthropus* (*7*).

Postcanine megadontia	Small anterior dentition	Large masticatory musculature	Current model
Large mandibular cross-sectional area at M_1	Nasoalveolar clivus concave in coronal plane	Thick zygomatic arch	Smooth entrance to nasal cavity
Wide mandibular extramolar sulcus	Incisor alveoli do not project beyond bicanine line	Anteriorly placed zygomatic	Thick palate
Large premolar area		Masseteric tubercle at or anterior to sellion	Low infraorbital foramen
Distinct dM_1 morphology		Strong anteromedial incursion of the temporal lines	Face hafted high
Molar and premolar cusp apices narrowly separated		Extensive overlap of squamosal suture	Marked postorbital constriction
Hyperthick enamel		Mastoid process inflated lateral to the supramastoid crest	
		Wide supraglenoid gutter	

extends onto the nasal surface of the premaxilla (Fig. 4B) (*23*). This configuration constrains the nasal surface of the hard palate to maintain the same transverse level as the adjacent premaxilla throughout growth (*21*). As a consequence, all resorption of the anterior nasal cavity floor would cease once the allowable limits of resorption of the premaxilla were reached. With inferior drift of its nasal surface thus limited, continued inferior drift of the hard palate's oral surface (in response to extreme maxillary rotation) would result in the consistent development of a greatly thickened hard palate (Fig. 4B).

The attachment of the vomer along the nasal cavity floor, through its influence on the pattern of nasal floor remodeling, may therefore be the pivotal factor responsible for the divergent palatal morphologies characteristic of australopithecine taxa (*17*). However, is the vomer's influence on australopithecine cranial morphology confined to the subnasal region? Probably not. If the model of australopithecine palatal development described above is indeed correct (*24*), then substantial downward remodeling of the nasal cavity floor in the robust specimens could not have occurred (Fig. 4B). Instead, continued expansion of the nasal cavity would set up a competition between the nasal and oral cavities for space within the midfacial skeleton. When such competition exists, an additional displacement must take place until the positions of the competing elements become sufficiently modified (*13*). In the robust australopithecine cranium, the point of contact of the two expanding elements would have been the nasal cavity floor (Fig. 4B). From this interface, the oral cavity would have been displaced inferiorly and the nasal cavity superiorly. Because the circumorbital elements are intimately associated with the perpendicular plate of the ethmoid, superior displacement of the nasal cavity would secondarily displace the entire circumorbital region superiorly.

With a displacement of the oral and orbito-nasal skeletons in opposite directions, any structures that span their connecting interface, such as the infraorbital region, must be vertically elongated. Also expected with a relatively greater superior displacement of the upper facial skeleton would be a higher hafting of the facial skeleton onto the neurocranium and a corresponding low frontal region. Strong postorbital constriction and a low position of the infraorbital foramina within the face would also be expected with such displacement of the upper face relative to the neural capsule. A suite of features can therefore be identified as the expected morphological correlates of a pattern of facial ontogeny in which the oral and upper facial capsules are displaced relative to a more stationary nasal cavity floor.

Table 1 lists the shared derived features of robust australopithecine crania as identified in a recent cladistic analysis (*7*). Most of these 20 traits are simply the most divisible elements of the more comprehensive masticatory features of (i) postcanine megadontia, (ii) a small anterior dentition, and, (iii) a large masticatory musculature. However, a number are not readily interpretable with respect to the masticatory apparatus. But, as has been demonstrated here, all are interpretable with respect to just two features of the robust australopithecine cranium: (i) a tall mandibular ramus and (ii) a vomeral insertion on the nasal surface of the premaxilla. The first is known to be functionally integrated with the postcanine occlusal area (*25*). The underlying basis of the second feature has yet to be explored, but it is critical to note that a similar vomeral insertion is found in modern humans (*17*, *21*), and we share with the robust australopithecines a relatively small anterior dentition. It therefore seems reasonable to suggest that the vomeral morphologies of both groups reflect a small anterior dentition. If so, and if the model of robust australopithecine craniofacial morphogenesis outlined above is correct, then all of the skeletal traits identified as synapomorphies of a *Paranthropus* clade are merely developmental by-products of dental size and proportions.

Although all robust australopithecines combine extremely large postcanine teeth with small anterior dentitions, they do not share identical tooth morphologies. Rather, *A. boisei* exhibits a number of non–size-related features of its postcanine dentition (for example, distinctive morphology of the lower fourth premolar and distinct lower molar cusp proportions) that are not observed in *A. robustus* (*2*). In addition, the postcanine teeth of *A. robustus* are notably smaller than those of both of the geologically older East African taxa. Although it is possible that a reduction in postcanine tooth size occurred during the evolution of *A. robustus* (*2*), it is no less probable that the East and South African forms had separate phyletic origins. Therefore, despite their fundamentally similar cranial morphologies, the phylogenetic history of the robust australopithecines remains unresolved.

References and Notes

1. E. Delson, in *The Evolutionary History of the "Robust" Australopithecines*, F. E. Grine, Ed. (de Gruyter, New York, 1988), pp. 317–324.
2. G. Suwa, T. D. White, F. C. Howell, *Am. J. Phys. Anthropol.* **101**, 247 (1996).
3. P. V. Tobias, *Olduvai Gorge: The Cranium of Australopithecus (Zinjanthropus) boisei* (Cambridge Univ. Press, Cambridge, 1967).
4. T. D. White, D. C. Johanson, W. H. Kimbel, *S. Afr. J. Sci.* **77**, 445 (1981).
5. B. A. Wood, *Koobi Fora Research Project, Volume 4, Hominid Cranial Remains from Koobi Fora* (Clarendon Press, Oxford, 1991); T. G. Bromage, F. Schrenk, F. W. Zonneveld, *J. Hum. Evol.* **28**, 71 (1995).
6. D. E. Lieberman, B. A. Wood, D. R. Pilbeam, *J. Hum. Evol.* **30**, 97 (1994).
7. D. S. Strait, F. E. Grine, M. A. Moniz, *ibid.* **32**, 17 (1997).
8. S. F. Gilbert, J. M. Opitz, R. A. Raff, *Dev. Biol.* **173**, 357 (1996).
9. R. A. Raff, *The Shape of Life. Genes, Development, and the Evolution of Animal Form* (Univ. of Chicago Press, Chicago, IL, 1996).
10. C. J. van der Klaauw, *Arch. Neerl. Zool.* **9**, 1 (1948–1952); M. L. Moss and R. W. Young, *Am. J. Phys. Anthropol.* **18**, 281 (1960); M. L. Moss and L. Salentijn, *Am. J. Orthod.* **55**, 567 (1969); *ibid.* **56**, 475 (1969); M. L. Moss, *Am. J. Orthod. Dentofacial Orthop.* **112**, 8 (1997); *ibid.*, p. 221; *ibid.*, p. 338; *ibid.*, p. 410.
11. C. Gans, *Development* **103** (suppl.), 3 (1988).
12. M. R. Kean and P. Houghton, *Anat. Rec.* **218**, 107 (1987).
13. D. H. Enlow and M. G. Hans, *Essentials of Facial Growth* (Saunders, Philadelphia, PA, 1996).

14. M. L. Moss and S. N. Greenberg, *Angle Orthod.* **37**, 151 (1967).
15. Y. Rak, *The Australopithecine Face* (Academic Press, New York, 1983).
16. M. L. Moss, *Acta Anat.* **44**, 263 (1961); S. W. Herring, *ibid.* **83**, 222 (1972); C. Katsaros, S. Killiardis, R. Berg, *Eur. J. Orthod.* **16**, 353 (1994).
17. M. A. McCollum, *Am. J. Phys. Anthropol.* **103**, 375 (1997).
18. A. Björk and V. Skieller, in *Factors Affecting the Growth of the Midface*, Monograph 6, *Craniofacial Growth Series*, J. A. McNamara Jr., Ed. (University of Michigan, Ann Arbor, MI, 1976), pp. 61–99; J. A. McNamara Jr., M. L. Riolo, D. H. Enlow, *Am. J. Phys. Anthropol.* **44**, 15 (1976); L. A. Bravo, I. L. Nielsen, A. J. Miller, *Am. J. Orthod. Dentofacial Orthop.* **96**, 26 (1989); E. D. Schneiderman, *Facial Growth in the Rhesus Monkey* (Princeton Univ. Press, Princeton, NJ, 1992).
19. T. G. Bromage, *J. Hum. Evol.* **18**, 751 (1989).
20. M. A. McCollum, *Am. J. Phys. Anthropol.* **93**, 259 (1994).
21. M. A. McCollum and S. C. Ward, *ibid.* **102**, 377 (1997).
22. G. C. Conroy and M. W. Vannier, *Nature* **329**, 625 (1987).
23. J. T. Robinson, *Am. J. Phys. Anthropol.* **12**, 181 (1954).
24. This model of robust australopithecine craniofacial morphogenesis predicts that the palatal component of the anterior nasal floor in *A. africanus* will display evidence of extensive resorption throughout growth. In the robust australopithecines, this same region should demonstrate reduced resorption later in cranial ontogeny. The predictions of this model are being assessed through scanning electron microscopic examination of the nasal cavity floor of juvenile australopithecine crania (*19*).
25. S. C. Ward and S. Molnar, *Am. J. Phys. Anthropol.* **53**, 383 (1980).
26. I thank O. Lovejoy, T. White, G. Suwa, and T. Bromage for comments on the manuscript, D. Knopsnyder for assistance with the graphics, and L. Gudz for providing original artwork. This research was supported by grants from Sigma Xi and the Boise Fund.

3 November 1998; accepted 3 March 1999

Solar Cycle Variability, Ozone, and Climate

Drew Shindell,[1]* David Rind,[1] Nambeth Balachandran,[1] Judith Lean,[2] Patrick Lonergan[3]

Results from a global climate model including an interactive parameterization of stratospheric chemistry show how upper stratospheric ozone changes may amplify observed, 11-year solar cycle irradiance changes to affect climate. In the model, circulation changes initially induced in the stratosphere subsequently penetrate into the troposphere, demonstrating the importance of the dynamical coupling between the stratosphere and troposphere. The model reproduces many observed 11-year oscillations, including the relatively long record of geopotential height variations; hence, it implies that these oscillations are likely driven, at least in part, by solar variability.

It has long been speculated that long-term solar output variations influence Earth's climate and may have caused episodes such as the Little Ice Age. As surface temperatures have risen rapidly over recent decades, it has become increasingly crucial to determine the relative importance of solar variation on climate. A first step is understanding the effects of the well-observed 10- to 12-year activity cycle. Although many meteorological quantities are correlated with the solar cycle (*1, 2*), it has remained unclear how relatively small changes in solar radiation (~0.1%), whose direct effects occur predominantly in the upper atmosphere, could have an important impact on Earth's surface. Cosmic ray influence on clouds has been proposed (*1*); others have suggested that the variability reflects other influences such as volcanoes (*3*) or internal climate oscillations (*4*). Another proposed mechanism is amplification of solar variability via stratospheric or thermospheric changes (*5, 6*). Measurements show that 10 to 20% of solar cycle irradiance changes occur in ultraviolet (UV) radiation (*7*), which is largely absorbed by stratospheric ozone.

A problem has been that most models with which this question has been studied have had limited stratospheric representations, have assumed a constant change in solar irradiance at all wavelengths, or have assumed constant ozone concentrations (*8–10*). Results showed that UV absorption changes altered the upper stratospheric zonal wind, which in turn affected planetary wave propagation and hence the troposphere. However, surface changes were quite small unless input solar variation was unrealistically large. One recent model (*6*) showed that incorporating both realistic solar irradiance and ozone changes could increase the response to solar forcing, but this model extended only to the middle stratosphere (10 mbar), a limitation that restricted the model's ability to simulate planetary wave propagation (*11*).

Here, we include both realistic irradiance and ozone changes in a climate model with a complete stratosphere. We used the GISS stratospheric general circulation model (GCM), a primitive equation model including parameterized gravity waves (*10*), with 8° latitude by 10° longitude resolution and 23 levels extending from the surface to 85 km (0.002 mbar). The two-dimensional (2D) model–derived chemistry parameterization includes wavelength-dependent ozone response to changes in radiation and temperature (*12*). Solar variability directly affects both ozone photochemistry and local heating, modifying ozone abundances, which in turn further alter local heating rates as well as the radiation field at other levels.

The GCM was run for 20 years each at solar maximum and solar minimum irradiances specified by wavelength-dependent changes from 180 to 400 nm, and constant changes at longer wavelengths consistent with total solar cycle irradiance variations (*7*). Results were analyzed in two ways: for the entire 40 years, and for a subset of the 28 years without sudden stratospheric warmings. The model showed no significant difference in generation of sudden warmings between phases, in accordance with observations (*13*). A companion experiment used identical radiation changes and constant ozone. All simulations had fixed sea-surface temperatures and no quasi-biennial oscillation (that is, the model was in its base state with weak easterlies).

Geopotential heights are controlled by temperatures in the underlying column, in addition to surface pressures, and thus height changes reflect temperature modification throughout the atmosphere below. An observed 10- to 12-year oscillation is present in more than 40 years of data (*2, 14*). Heights from about 10° to 50°N are well correlated with solar flux [>99.9% significance at 30 mbar for the annual average zonal mean (*2*)]. We concentrate on December through February, when differences in observed height changes between Northern Hemisphere subtropical and high latitudes are the greatest (between 30° and 90°N, a change of 104 m in winter versus 33 m in summer).

The individual years of the solar maximum and minimum simulations were averaged to reduce the noise, then the difference between them was calculated. The zonal mean 30-mbar height changes showed significant increases at low and mid-latitudes (Fig. 1). An additional experiment with ozone changes prescribed according to observations gave a similar response to that with calculated ozone, indicating the robustness of the result. The models with solar forcing and interactive ozone reproduce observed Northern Hemisphere subtropical height increases well, but the model with solar forcing and with constant ozone does not. For compari-

---

[1] NASA Goddard Institute for Space Studies (GISS) and Center for Climate Systems Research, Columbia University, 2880 Broadway, New York, NY 10025, USA. [2] E. O. Hulburt Center for Space Research, Naval Research Laboratory, Washington, DC 20375, USA. [3] Space Science and Applications Inc., 2880 Broadway, New York, NY 10025, USA.

*To whom correspondence should be addressed. E-mail: dshindell@giss.nasa.gov